Dislocation-induced breakthrough of strength and ductility trade-off in a non-equiatomic high-entropy alloy

Guo, Wenqi; Su, Jing; Lu, Wenjun; Liebscher, Christian H.; Kirchlechner, Christoph; Ikeda, Yuji; Körmann, Fritz; Liu, Xuan; Xue, Yunfei; Dehm, Gerhard

DOI
10.1016/j.actamat.2019.11.055

Publication date
2020

Document Version
Final published version

Published in
Acta Materialia

Citation (APA)
Guo, W., Su, J., Lu, W., Liebscher, C. H., Kirchlechner, C., Ikeda, Y., Körmann, F., Liu, X., Xue, Y., & Dehm, G. (2020). Dislocation-induced breakthrough of strength and ductility trade-off in a non-equiatomic high-entropy alloy. *Acta Materialia*, *185*, 45-54. https://doi.org/10.1016/j.actamat.2019.11.055

Acta Materialia 185 (2020) 45–54

Contents lists available at ScienceDirect

Acta Materialia

journal homepage: www.elsevier.com/locate/actamat

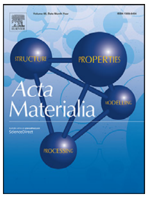

Full length article

Dislocation-induced breakthrough of strength and ductility trade-off in a non-equiatomic high-entropy alloy

Wenqi Guo[a], Jing Su[a], Wenjun Lu[a,*], Christian H. Liebscher[a,*], Christoph Kirchlechner[a], Yuji Ikeda[a], Fritz Körmann[a,b], Xuan Liu[c], Yunfei Xue[c], Gerhard Dehm[a,*]

[a] *Max-Planck-Institut für Eisenforschung GmbH, Max-Planck-Straße 1, 40237 Düsseldorf, Germany*
[b] *Materials Science and Engineering, Delft University of Technology, 2628 CD Delft, the Netherlands*
[c] *School of Materials Science and Engineering, Beijing Institute of Technology, Beijing 100081, China*

ARTICLE INFO

Article history:
Received 17 September 2019
Revised 20 November 2019
Accepted 21 November 2019
Available online 30 November 2019

Keywords:
High-entropy alloy
Stacking fault energy
Grain refinement
Strength-ductility trade-off
Dislocation

ABSTRACT

In conventional metallic materials, strength and ductility are mutually exclusive, referred to as strength-ductility trade-off. Here, we demonstrate an approach to improve the strength and ductility simultaneously by introducing micro-banding and the accumulation of a high density of dislocations in single-phase high-entropy alloys (HEAs). We prepare two compositions ($Cr_{10}Mn_{50}Fe_{20}Co_{10}Ni_{10}$ and $Cr_{10}Mn_{10}Fe_{60}Co_{10}Ni_{10}$) with distinctive different stacking fault energies (SFEs) as experimental materials. The strength and ductility of the $Cr_{10}Mn_{50}Fe_{20}Co_{10}Ni_{10}$ HEA are improved concurrently by grain refinement from 347.5 ± 216.1 µm to 18.3 ± 9.3 µm. The ultimate tensile strength increases from 543 ± 4 MPa to 621 ± 8 MPa and the elongation to failure enhances from 43±2% to 55±1%. To reveal the underlying deformation mechanisms responsible for such a strength-ductility synergy, the microstructural evolution upon loading is investigated by electron microscopy techniques. The dominant deformation mechanism observed for the $Cr_{10}Mn_{50}Fe_{20}Co_{10}Ni_{10}$ HEA is the activation of micro-bands, which act both as dislocation sources and dislocation barriers, eventually, leading to the formation of dislocation cell structures. By decreasing grain size, much finer dislocation cell structures develop, which are responsible for the improvement in work hardening rate at higher strains (>7%) and thus for the increase in both strength and ductility. In order to drive guidelines for designing advanced HEAs by tailoring their SFE and grain size, we compute the SFEs of $Cr_{10}Mn_xFe_{70-x}Co_{10}$Ni10 ($10 \leq x \leq 60$) based on first principles calculations. Based on these results the overall changes on deformation mechanism can be explained by the influence of Mn on the SFE.

1. Introduction

Conventional alloy design strategies are mostly based on one principal element with the addition of several other minor elements with the aim to improve the mechanical properties and performance of the material [1]. In recent years, a novel alloy design concept has drawn great attention, where multi-principal elements are mixed at equiatomic or near equiatomic concentrations to form highly concentrated solid solutions, termed high-entropy alloys (HEAs) [2–5]. To promote the wide use of HEAs as structural materials, it is highly desirable to improve the strength of HEAs while maintaining good ductility. Grain refinement is an important way to improve the mechanical strength, but for most metals and alloys, grain refinement results in a reduction in ductility [6]. Over the past decades, numerous approaches have been developed to effectively strengthen metallic materials without significantly sacrificing ductility (e.g., nanotwins [7], heterogeneous structures [8] and phase transformations [9–11]), and to reveal the underlying deformation mechanisms [11]. Li et al. [12] showed that both strength and ductility can be increased in a dual-phase HEA, consisting of face-centered cubic (FCC) matrix and hexagonal close-packed (HCP) phase, by decreasing grain size. This is mainly attributed to the low stacking fault energy (SFE) of the dual-phase HEA and thus the activation of deformation-induced displacive phase transformation, i.e., from FCC to HCP phase, upon straining [12].

The stacking fault energy (SFE) of FCC based alloys is found to greatly affect the activation of plastic deformation modes, such as, dislocation slip, mechanical twinning and phase transformations. Therefore, it impacts the work hardening ability and thus the mechanical properties of the alloys [13–15]. Typically, for FCC

---

[*] Corresponding authors.
E-mail addresses: guowenqi1988520@outlook.com, 794477343@qq.com (W. Guo), w.lu@mpie.de (W. Lu), liebscher@mpie.de (C.H. Liebscher), dehm@mpie.de (G. Dehm).

https://doi.org/10.1016/j.actamat.2019.11.055

metals and alloys a particular range in SFE correlates with a dominant deformation mechanism: ~15 mJ/m^2 $<$ SFE $<$ 50 mJ/m^2 for twinning, SFE $<$ 15–18 mJ/m^2 for phase transformation, and 50 mJ/m^2 $<$ SFE for dislocation slip-based plasticity [16]. Compared to equiatomic HEAs, non-equiatomic HEAs greatly expand the compositional space, as well as the accessible range in SFE [17,18]. Thus, the design of non-equiatomic HEAs provides effective ways to obtain alloys with controllable SFE and hence tunable mechanical properties. Recently, phase-transformation-induced plasticity (TRIP) dual-phase HEAs with low SFE were developed in the CrMnFeCo system and the bidirectional transformation of FCC and HCP offers an extensive work hardening capacity without sacrificing ductility [18,19]. In addition, Cai et al. [19] studied the influence of Mo additions on the deformation mechanisms of a CrFeCoNi HEA with an estimated SFE of ~19 mJ/m^2. The microstructure of this HEA contains both nano-twins and microbands, which result in a good combination of strength and ductility.

Up to now, many studies focused on the influence of SFE on the hardening capability of HEA [20–23], but only few studies investigated how the trade-off between strength and ductility could be overcome in FCC based HEAs by also considering dislocation plasticity. In high Mn steels, micro-banding induced plasticity has been reported to be responsible for the improvement in the work hardening ability [24]. Besides, Welsch et al. [25] found that microbands developed from the slip bands filled with dislocations via planar slip in Fe-30.4Mn-8Al-1.2C (wt.%) steel with a high SFE of 85 mJ/m^2. Thus, FCC HEAs with tunable SFE are interesting candidates to investigate which deformation mechanism could be utilized to optimize strength and ductility simultaneously.

In this study, we first designed two non-equiatomic FCC based HEAs with five principle elements (i.e., Cr, Mn, Fe, Co, and Ni). The designed $Cr_{10}Mn_{10}Fe_{60}Co_{10}Ni_{10}$ HEA shows a dislocation dominated deformation mechanism, whereas in the $Cr_{10}Mn_{50}Fe_{20}Co_{10}Ni_{10}$ HEA twinning-induced plasticity is the major deformation mode. The effect of grain size on the tensile strength and ductility of the two HEAs was studied systematically. The influence of the Mn content on the SFE energy was further investigated by first-principles calculations for the composition range $Cr_{10}Mn_xFe_{70-x}Co_{10}Ni_{10}$ $(10 \leq x \leq 60)$ to support the microstructural observations. The effect of the SFE on the deformation mode of single FCC phase HEAs is discussed in detail.

2. Methodology

2.1. Alloy compositions and thermomechanical processing design

The nominal compositions of the two designed non-equiatomic HEAs are $Cr_{10}Mn_{50}Fe_{20}Co_{10}Ni_{10}$ (D-HEA: dislocation dominated-high entropy alloy) and $Cr_{10}Mn_{10}Fe_{60}Co_{10}Ni_{10}$ (NT-HEA: nano-twinning dominated-high entropy alloy). Both alloys were cast in a vacuum induction furnace using pure metals (99.9%). The as-cast ingots were hot-rolled at 900 °C to a thickness reduction of 50% (from 10 mm to 5 mm). Subsequently, the alloy sheets were homogenized at 1100 °C (D-HEA) and 1300 °C (NT-HEA) for 2 h in Ar protected atmosphere followed by water quenching. The melting points of both HEAs were measured by differential scanning calorimetry (DSC) in a NETZSCH STA 449 F3 instrument. Both heating rate and cooling rate are 10 °C/min, and 2 cycles were conducted for each specimen. The homogenization temperatures were chosen to ~100 °C below their melting points to fully dissolve the as-cast dendrites and get an adequately homogenous chemical distribution. In this way, coarse-grained (CG) microstructures also formed. For the fabrication of fine-grained (FG) microstructures, the homogenized sheets were subjected to cold rolling to a thickness reduction of 60% (from 5 mm to 2 mm) and subsequent annealing at the temperature of 900 °C for 3 min followed by water quenching. The measured chemical compositions of both HEAs by wet chemical analysis are given in Table 1.

Table 1
Wet chemical analysis of two HEAs. FG and CG refer to fine grain and coarse grain, respectively.

Sample	Cr (at.%)	Mn (at.%)	Fe (at.%)	Co (at.%)	Ni (at.%)
D-HEA (Cast)	10.20	48.79	20.97	10.00	10.04
D-HEA (CG)	9.96	48.88	21.69	9.81	9.76
D-HEA (FG)	9.99	49.19	21.07	9.91	9.85
NT-HEA (Cast)	10.00	9.83	60.37	9.88	9.92
NT-HEA (CG)	9.91	9.77	60.62	9.88	9.82
NT-HEA (FG)	9.96	9.81	60.44	9.88	9.92

Dog-bone shaped tensile specimens (CG and FG) with gauge dimension of 1 × 10 × 2 mm^3 were cut by electrical discharge machining. The uniaxial tensile test was performed using a Kammrath & Weiss tensile stage with the assistance of digital image correlation (DIC) technique. Three specimens were tested with a strain rate of 0.0025 s^{-1} at ambient temperature for each state (NT-CG, NT-FG, D-CG, D-FG). The cross-section of the fractured tensile sample was mounted to analyze the deformed microstructure. The sample surface was mechanically ground with silicon carbide abrasive paper (P60 to P4000), and then polished by using 3 and 1 µm diamond suspensions. Fine polishing was performed by using 50 nm SiO_2 suspension to remove the deformation layer on the surface.

2.2. Microstructure characterization

The global crystal structure of two alloys was measured by X-ray diffraction (XRD) using ISO-DEBYEFLEX 3003 with a Co-Kα (λ = 1.79 Å) source operating at 40 kV and 40 mA. XRD data was recorded between 20 and 130° (2θ) at a step size of 0.03° and a counting time of 30 s. Electron backscatter diffraction (EBSD) measurements were carried out using a JEOL 6490 scanning electron microscope (SEM). Electron channeling contrast imaging (ECCI) analysis was performed in a Zeiss-Merlin instrument. Transmission electron microscopy (TEM) samples were prepared using mechanical polishing followed by electro-polishing in an electrolyte of 95% acetic acid and 5% perchloric acid. The electro-polishing was conducted at the voltage of 34 V at room temperature. Scanning TEM (STEM) was conducted in an aberration-corrected FEI Titan Themis 80–300 at an acceleration voltage of 300 kV. For low angle annular dark-field (LAADF) imaging, a probe semi-convergence angle of 17 mrad and inner and outer semi-collection angles from 14 mrad to 63 mrad were utilized [17].

2.3. First-principles calculations

First-principles calculations were employed to study the effect of Mn content on the SFE of the non-equiatomic HEAs. The electronic structure calculations were performed with the exact-muffin-tin-orbital (EMTO) method [26–30] in combination with the full-charge-density (FCD) method [31,32] within the density functional theory (DFT) framework. The charges and energies were calculated within the generalized gradient approximation (GGA) of the Perdew–Burke–Ernzerhof (PBE) form [33]. Ideal mixing of the chemical elements was modeled based on the coherent potential approximation (CPA) [34–36]. The Brillouin zones were sampled by the meshes with more than 10,000 k-points per atom. Note that total energies of 3d-transition-element HEAs often strongly depend on the magnetic state [37,38].

The intrinsic SFEs of FCC alloys were computed based on the first-order axial Ising model (AIM1) [39–41] as

$$\gamma_{\mathrm{ISF}} \approx \frac{2\left(E^{\mathrm{HCP}} - E^{\mathrm{FCC}}\right)}{A} \tag{1}$$

Table 2
Parameters calculated according to XRD measurements. a is the crystal lattice, ε is the microstrain, ρ is the dislocation density, and $\Delta\sigma$ is the estimated increased strength.

	Local Strain (%)	a (nm)	ε	ρ (m^{-2})	$\Delta\sigma$ (MPa)
D-HEA(CG)	~40	0.3636	0.094	1.6 × 1013	46
D-HEA(CG)	~80	0.3633	0.099	1.7 × 1013	47
D-HEA (FG)	~40	0.3635	0.099	1.5 × 1014	141
D-HEA (FG)	~80	0.3634	0.100	1.6 × 1014	142
NT-HEA(CG)	~40	0.3586	0.074	8.1 × 1012	33
NT-HEA (CG)	~80	0.3585	0.095	1.0 × 1013	37
NT-HEA (FG)	~40	0.3586	0.074	9.6 × 1013	113
NT-HEA (FG)	~80	0.3586	0.133	1.7 × 1014	150

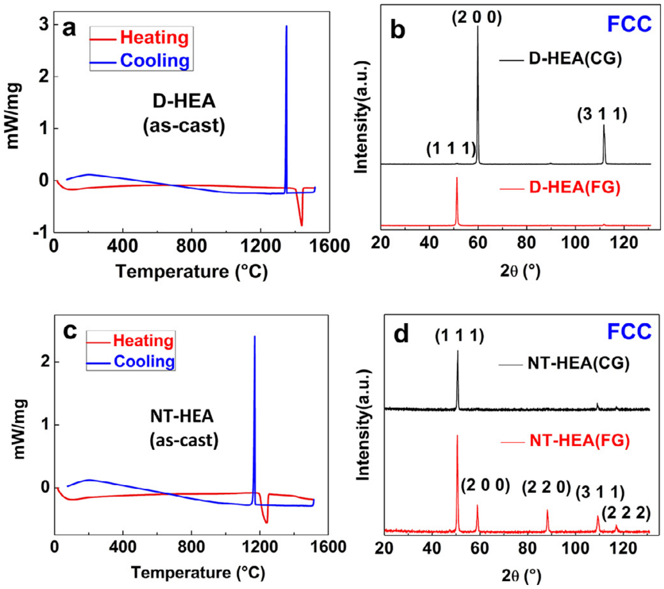

Fig. 1. DSC results of the as-cast (a) $Cr_{10}Mn_{50}Fe_{20}Co_{10}Ni_{10}$ (D-HEA: dislocation dominated-high entropy alloy); (c) $Cr_{10}Mn_{10}Fe_{60}Co_{10}Ni_{10}$ (NT-HEA: nano-twinning dominated-high entropy alloy); XRD result of the as-cast (b) $Cr_{10}Mn_{50}Fe_{20}Co_{10}Ni_{10}$ D-HEA; (d) $Cr_{10}Mn_{10}Fe_{60}Co_{10}Ni_{10}$ NT-HEA. FG and CG describe the fine grain and coarse grain.

where A denotes the area per atom, and E^{α} denotes the energy per atom of the phase α. We confirmed that for the present application the second-order axial Ising model (AIM2) [39] as well as models with explicit ISFs show the same qualitative trend as that of the AIM1. The total energies of the FCC and the HCP phases in Eq. (1) are computed with their one- and two-atom primitive cells, respectively. The volumes per atom were fixed to the ones interpolated or extrapolated from the values of the FCC phases in the present experiments (see Table 2). The ideal c/a ratio of $\sqrt{8/3} \approx 1.633$ was applied to the HCP phase. Internal atomic positions were fixed to keep the rigid-sphere packing.

3. Results

3.1. Initial microstructure

The thermal stability and the initial microstructure of the alloys were characterized by DSC, XRD and EBSD. Figs. 1(a) and (c) show the DSC results of the as-cast D-HEA and NT-HEA, respectively. The average melting temperature of the D-HEA and NT-HEA is 1197 °C and 1407 °C, respectively. The heating curves don't reveal any extra peaks before melting or after solidification for both alloys. This indicates that there is no obvious phase transition occurring before melting or after solidification. From the XRD analysis (Figs. 1(b) and (d)), only the face-centered cubic (FCC) phase is detected in both HEAs with coarse and fine grains. A single FCC phase forms in both alloys after hot rolling and homogenization. When subjected to further cold rolling and annealing, both HEAs keep the FCC phase and no phase transformation is detected.

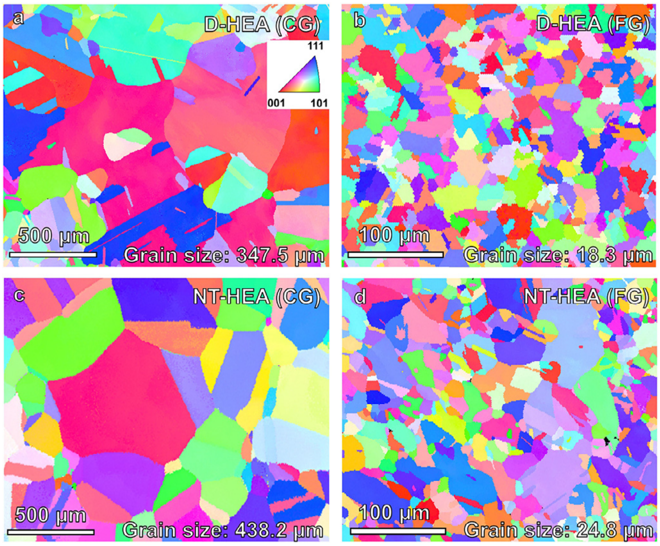

Fig. 2. EBSD IPF maps of (a) $Cr_{10}Mn_{50}Fe_{20}Co_{10}Ni_{10}$ D-HEA with coarse grain (CG); (b) $Cr_{10}Mn_{50}Fe_{20}Co_{10}Ni_{10}$ D-HEA with fine grain (FG); (c) $Cr_{10}Mn_{10}Fe_{60}Co_{10}Ni_{10}$ NT-HEA (CG); (d) $Cr_{10}Mn_{10}Fe_{60}Co_{10}Ni_{10}$ NT-HEA (FG).

Fig. 2 shows the inverse pole figure (IPF) maps of the two HEAs with different grain sizes. For the D-HEA alloy, the average grain size is determined to be 347.5 ± 216.1 μm, as shown in Fig. 2(a). After cold rolling and annealing, the microstructure is fully recrystallized, resulting in a refined grain structure with an average size of 18.3 ± 9.3 μm (Fig. 2(b)). Similarly, the average grain sizes of coarse- and fine-grained NT-HEA are 438.2 ± 300.7 μm and 24.8 ± 14.6 μm, respectively (Fig. 2(c) and (d)). Annealing twins are also observed in both coarse- and fine-grained structures. Compared to the D-HEA (FG) alloy, the grain size distribution of the NT-HEA (FG) alloy is less homogeneous.

3.2. Mechanical properties

The mechanical properties at room temperature for the two HEAs with coarse and refined grain size have been determined by bulk tensile testing. Fig. 3(a) shows the engineering stress-strain curves of the two HEAs. The average yield strength (YS) and average ultimate tensile strength (UTS) of the D-HEA (CG) are 248 ± 8 MPa and 543 ± 4 MPa, respectively, and the fracture strain is 43 ± 2%. After grain refinement, it is interesting that both strength and ductility show an increasing tendency. The average YS and UTS increase to 341 ± 10 MPa and 621 ± 8 MPa, with an increase of 37.5% and 14.3%. Meanwhile, the fracture strain of D-HEA (FG) is 55 ± 1%, with an increase being 27.9%. For NT-HEA, the YS and UTS of the NT-HEA (CG) are 170 ± 25 MPa and 521 ± 34 MPa, respectively. NT-HEA has better ductility than the D-HEA regardless of grain refinement. The NT-HEA (CG) has a fracture strain of about 78 ± 7%. In the fine-grained NT-HEA, the YS and UTS increase to 318 ± 18 MPa and 698 ± 8 MPa, with an increase of 87.0% and 34.0%. The fracture strain decreases to 70 ± 2%, with the loss of ductility being 11.4%. Fig. 3(b) shows the mechanical properties of the investigated HEAs in comparison to other HEAs and engineering alloys. Both, strength and ductility of D-HEA (FG) is higher than the equiatomic FCC HEAs ($Cr_{20}Mn_{20}Fe_{20}Co_{20}Ni_{20}$ [42]), and is also comparable to non-equiatomic FCC HEAs ($Cr_{10}Fe_{40}Mn_{40}Co_{10}$

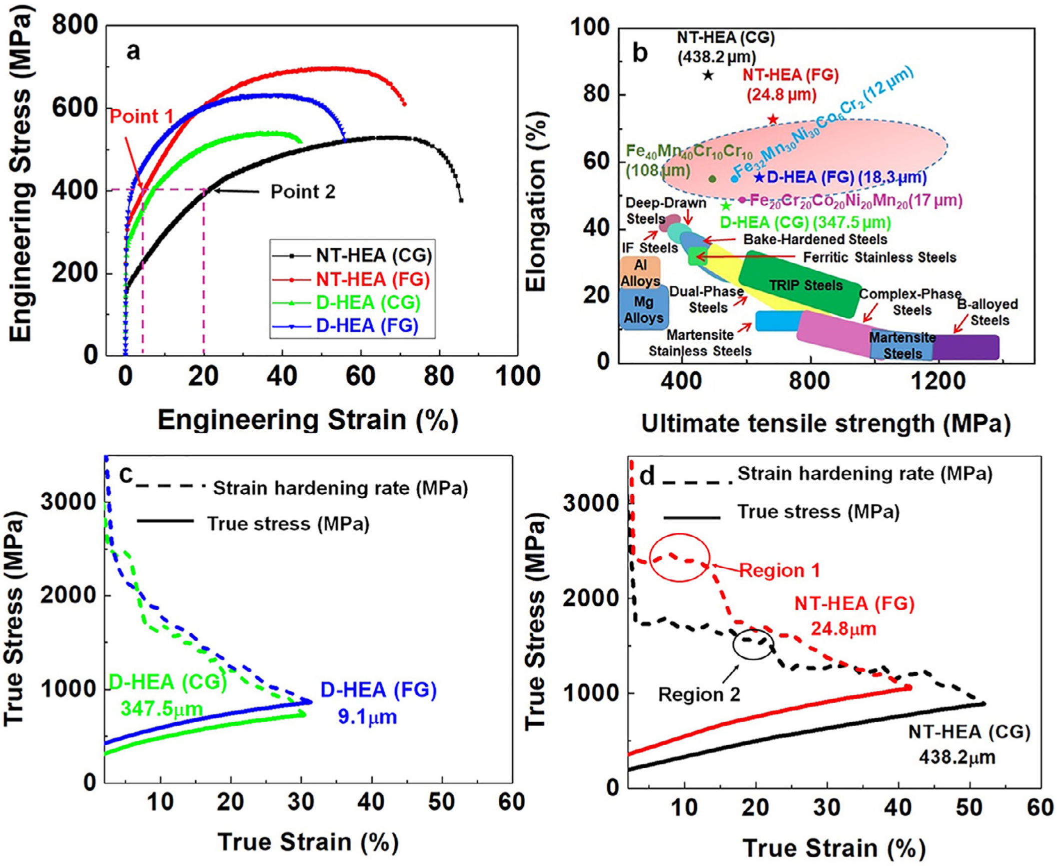

Fig. 3. (a) Tensile engineering stress-strain curves of two non-equiatomic HEAs; (b) mechanical behavior of current HEAs compared to other engineering alloys [29,30]; (c) and (d) strain hardening curves and true stress-strain curves of two HEAs. (For interpretation of the references to color in this figure legend, the reader is referred to the web version of this article.)

[43], $Cr_2Mn_{30}Fe_{32}Co_6Ni_{30}$ [43]). Figs. 3(c) and (d) exhibit true stress-true strain curves superimposed with their corresponding work hardening plots. At true strains above 7%, the fine-grained D-HEA displays a little higher work hardening rate than the coarse-grained D-HEA, as shown in Fig. 3(c). In contrast, the NT-HEA with refined grains exhibits a more pronounced strain hardening capability at small strains (5–15%) compared to that with coarse grains, as shown in region 1 in Fig. 3(d). The difference between the work hardening rates of the NT-HEA with different grain sizes converges at higher strains. The underlying deformation mechanisms will be discussed in detail.

3.3. Deformed microstructure and phase stability

Deformed microstructure, phase stability and dislocation density of the alloys were characterized and estimated by XRD and EBSD. Figs. 4(a1)–(d1) show the IPF map of the deformed HEAs with a local strain of 80% as determined by DIC (Appendix A). No deformation twins could be observed in the deformed $Cr_{10}Mn_{50}Fe_{20}Co_{10}Ni_{10}$ D-HEA, as shown in Figs. 4(a1), (b1), while a large amount of deformation twins forms in the deformed $Cr_{10}Mn_{10}Fe_{60}Co_{10}Ni_{10}$ NT-HEA, with the volume fraction of twins of NT-HEA (CG) and NT-HEA (FG) being 20.4% and 2.8%. Kernel average misorientation (KAM) maps with the first nearest-neighbor of the deformed HEA are shown in Figs. 4(a2)–(d2). High local misorientation values are observed in D-HEA, indicating a high dislocation density in areas with a local strain of 80%. For NT-HEA, in contrast, the local misorientation value remains lower in areas with a local strain of 80%, which can be seen in Fig. 4(c2) and Fig. 4(d2). Figs. 4(a3)–(d3) show the phase map as well as the twin boundary distribution of deformed HEAs, and twin boundary density is much lower in D-HEA.

Figs. 5(a) and (b) show the XRD results of the D-HEA in regions with different local strains. In the region of local strain of ~40% and ~80%, only FCC peaks are detected in the D-HEA (CG) and D-HEA (FG), and no other phases are detected. The condition is similar to the NT-HEA. In the region of local strain of ~40% and ~80%, only FCC peaks are detected in NT-HEA (CG) and NT-HEA (FG), indicating that within the resolution and detection limits of XRD, no phase transformation occurs during straining.

During plastic deformation, mobile dislocations can interact with each other and also impeding their own motion, contributing to strain hardening. The increase in yield strength due to dislocation reactions ($\Delta\sigma$) can be approximated as [44]:

$$\Delta\sigma = M\alpha Gb\rho^{0.5} \tag{2}$$

where $M = 3.06$ is the Taylor factor that converts shear stress to normal stress for FCC polycrystalline matrix, $\alpha = 0.2$ is a constant for FCC metals, $G = 74$ GPa is the shear modulus for the CrMnFeCoNi system. The dislocation density (ρ) can be estimated by the following equation [44]:

$$\rho = 2\sqrt{3}\varepsilon/(Db) \tag{3}$$

where ε is the microstrain, D is the grain size, and b is the Burgers vector. In the current work, the grain size ranges from ~20 μm to ~450 μm, and the grain size effect on XRD peak broadening is not taken into account. For an FCC structure, $b = (\frac{\sqrt{2}}{2})a$, where a is the lattice parameter of the FCC phase.

Table 2 shows the estimated data of dislocation density (ρ) and increased strength ($\Delta\sigma$) caused by dislocation based plasticity. For

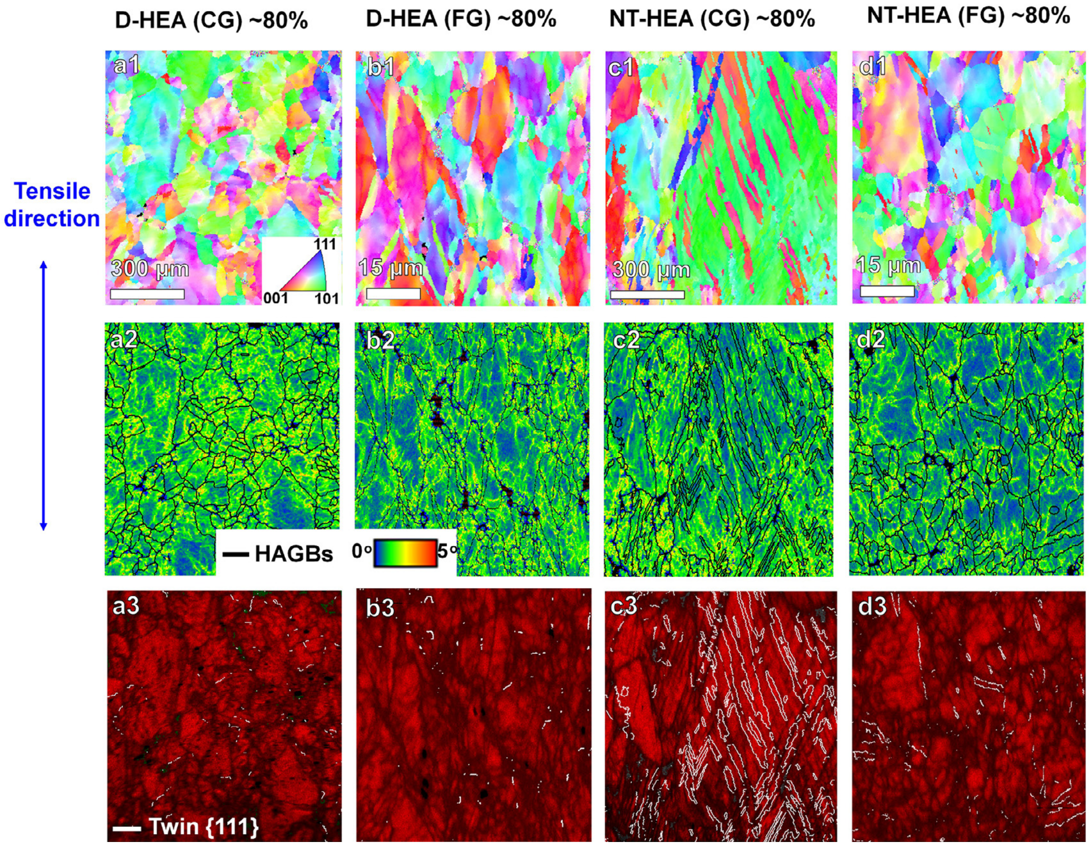

Fig. 4. EBSD results of the deformed HEAs with ~80% local strain. (a): $Cr_{10}Mn_{50}Fe_{20}Co_{10}Ni_{10}$ D-HEA with coarse grain (CG); (b): D-HEA with fine grain (FG); (c): $Cr_{10}Mn_{10}Fe_{60}Co_{10}Ni_{10}$ NT-HEA with coarse grain (CG); (d): NT-HEA with fine grain (FG): (1) IPF maps; (2) kernel average misorientation between 0 and 5°; (3) phase maps (the white color shows the twinning boungdaries).

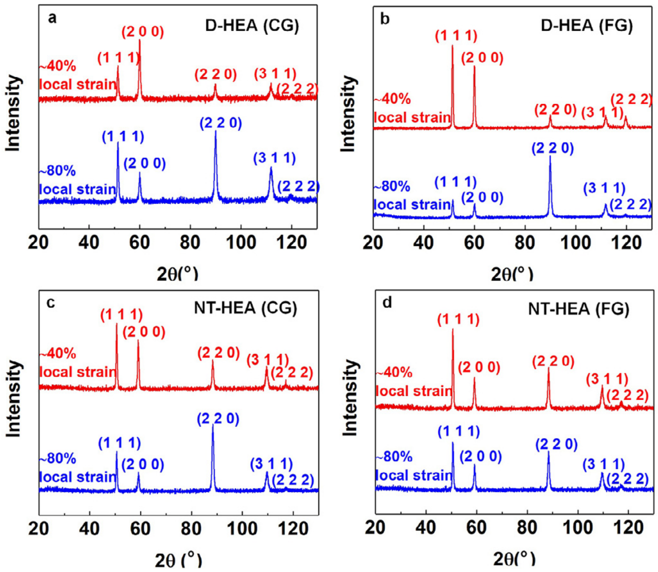

Fig. 5. XRD result of the deformed high entropy alloy with local strain of ~40% and ~80%: (a) $Cr_{10}Mn_{50}Fe_{20}Co_{10}Ni_{10}$ D-HEA with coarse grain (CG); and (b) with fine grain (FG); (c) $Cr_{10}Mn_{10}Fe_{60}Co_{10}Ni_{10}$ NT-HEA (CG); (d) NT-HEA (FG).

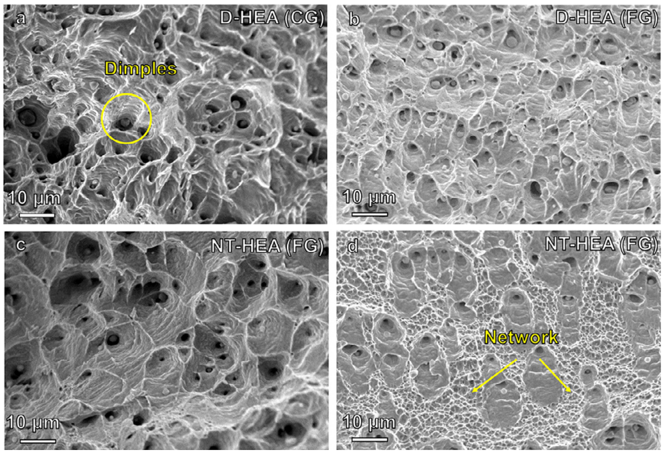

Fig. 6. Fracture morphologies of HEAs after tensile testing: (a) $Cr_{10}Mn_{50}Fe_{20}Co_{10}Ni_{10}$ D-HEA (Dislocation dominated-high entropy alloy) with coarse grain (CG); (b) D-HEA with fine grain (FG); (c) $Cr_{10}Mn_{10}Fe_{60}Co_{10}Ni_{10}$ NT-HEA (Twinning dominated-high entropy alloy) (CG); (d) NT-HEA (FG).

the D-HEA (CG), the dislocation density is 1.6×1013 m^{-2} with the local strain of ~40%, and the corresponding $\Delta\sigma$ is 46 MPa. After grain refinement, the dislocation density of D-HEA (FG) increases to 1.5×10^{14} m^{-2}, and the $\Delta\sigma$ also increases 141 MPa. Compared with D-HEA, NT-HEA has a lower dislocation density and lower $\Delta\sigma$ under the same strain condition. For NT-HEA (CG), when the local strain is ~40%, the dislocation density is 8.1×10^{12} m^{-2}, and $\Delta\sigma$ is calculated to be 33 MPa. After grain refinement, dislocation density increases to 9.6×10^{13} m^{-2} with the same local strain and the estimated $\Delta\sigma$ increases to 113 MPa.

3.4. Fractography

The fracture mode of the two HEAs was studied by inspecting fracture surfaces in the SEM after tensile testing. Figs. 6(a) and (b)

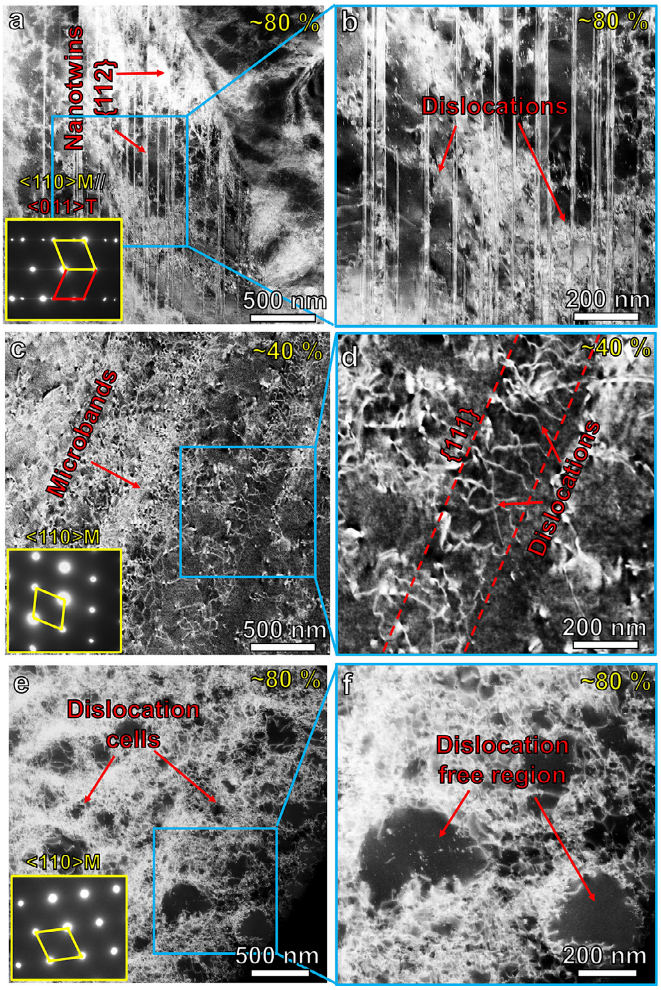

Fig. 7. Representative LAADF-STEM imagaes with local strain values: (a) and (b) ~80% in the $Cr_{10}Mn_{10}Fe_{60}Co_{10}Ni_{10}$ NT-HEA with fine grain (FG) structure; (c) and (d) ~40% in the $Cr_{10}Mn_{50}Fe_{20}Co_{10}Ni_{10}$ D-HEA (FG); (e) and (f) ~80% in the D-HEA (FG).

show the fracture morphologies of the D-HEA after tensile testing. Large numbers of dimples are observed, indicating that the fracture mode of D-HEA is a ductile fracture. The distribution of dimples keeps homogeneous after grain refinement. Particles are observed inside the voids of the fracture surface, which are identified to be inclusions acting as initiation sites for the formation of the voids [9]. The inclusions have qualitatively been identified as Mn-oxide by SEM-EDX. Similar to D-HEA, the fracture mode of NT-HEA is also ductile fracture, confirmed by the dimples observed in Figs. 6(c) and (d). Compared with NT-HEA (CG) alloy, the NT-HEA (FG) alloy has a heterogeneous distribution of dimples, and networks of dimples in the size range of 600~1200 nm. The heterogeneous distribution of dimples in NT-HEA (FG) alloy is related to the heterogeneous and hierarchical microstructure, which is beneficial to high strength [22].

3.5. Deformation mechanisms

In order to reveal the deformation mechanism of the two HEAs at the nanometer scale, TEM and STEM was used to analyze deformed microstrctures. Fig. 7(a) shows an overview of the deformed NT-HEA (FG) with a local strain of ~80% via LAADF-STEM imaging. The straight vertical lines within the matrix are coherent Σ3 twin boundaries parallel to {111} habit planes, also confirmed by selected area electron diffraction (SAED) from the same region as shown in the figure inset. In this SAED, only the twin reflections are visible without any signature of secondary phases. The enlarged LAADF-STEM view corresponding to the highlighted position in Fig. 7(a) is shown in Fig. 7(b). The average spacing of nanotwins in this region is determined to 18 ± 4 nm and in certain areas, bands with high dislocation density are observed. Similarly, LAADF-STEM imaging was also applied to characterize the deformed D-HEA (FG) with local strains of ~40% and 80%, are displayed in Figs. 7(c)–7(d) and 7(e)–7(f), respectively. In the state of ~40% local strain, deformation is observed to occur via the formation of aligned microbands with high dislocation density {111} habit plane and no indication for the formation of nanotwins is found (See Figs. 7(c) and 7(d)). After severe deformation with a local strain of ~80%, these deformation-induced microbands were completely changed to dislocation cells with a diameter range from ~50 nm to ~300 nm, as shown in Figs. 7(e) and 7(f).

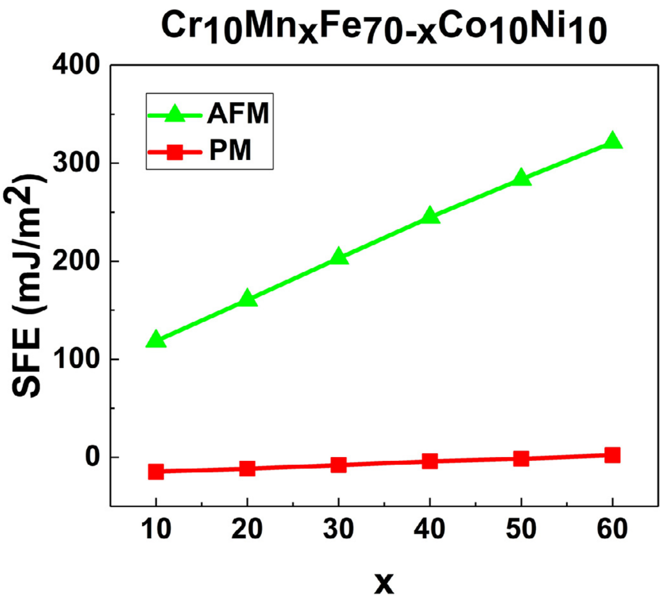

Fig. 8. SFEs of the investigated compositions obtained by first principles calculations. Squared red and green triangle symbols denote the results in the PM and the AFM states, respectively. (For interpretation of the references to color in this figure legend, the reader is referred to the web version of this article.)

4. Discussion

4.1. Effect of Mn content on stacking fault energy

The effect of the Mn content on the stacking fault energy can be used to explain the deformation behavior from an atomistic and energetic point of view. Here, we compute the SFEs of $Cr_{10}Mn_xFe_{70-x}Co_{10}Ni_{10}$ ($10 \leq x \leq 60$) based on first principles calculations. Since in experiments both the D-HEA ($Cr_{10}Mn_{50}Fe_{20}Co_{10}Ni_{10}$) and the NT-HEA ($Cr_{10}Mn_{10}Fe_{60}Co_{10}Ni_{10}$) are paramagnetic (PM) at room temperature, we first consider the PM state where the orientations of magnetic moments are randomly fluctuated due to thermal excitations. This is modeled employing the disordered local moment (DLM) [45,46] approach in which the magnetic fluctuation in the PM state is mimicked by an equal mixing of spin-up and the spin-down magnetic moments in the spirit of the CPA. The computed SFEs in the PM state are shown in Fig. 8 (square red symbols). In the PM state, the SFE is found to slightly decrease with decreasing Mn content. Specifically, from $Cr_{10}Mn_{50}Fe_{20}$ $Co_{10}Ni_{10}$ to $Cr_{10}Mn_{10}Fe_{60}Co_{10}Ni_{10}$ the SFE in the PM state decreases by approximately 10 mJ/m^2. Note that the absolute SFE values may be modified by e.g. finite-temperature excitations such as lattice vibrations [10,47,48] and by chemical fluctuations close to the stacking faults [49,50]. Such excitations usually induce a constant SFE shift, but do in practice normally not affect the overall chemical trends, in which we are mainly interested in the present work. We investigated different magnetic states as will be discussed below. The inclusion of further finite-temperature excitations is beyond the scope of the present work.

In a recent study for FCC $Cr_{20}Mn_xFe_yCo_{20}Ni_z$ ($x + y + z = 60$) [51], the antiferromagnetic (AFM) state with alternative magnetic orientations along the {100} direction is found to be energetically more stable than the previously-found ferrimagnetic (FiM) state [38] in a wide composition range. The magnetic transition temperatures T_c in the AFM state were also found close to room temperature particularly for high-Mn compositions, indicating that also magnetic short-range ordering (SRO) may remain and impact the energies at room temperature. Based on this finding, it was demonstrated that the magnetic state could, in principle, also affects the chemical trends of SFEs. We therefore also consider the AFM state as well as the FiM state for the present FCC $Cr_{10}Mn_xFe_{70-x}Co_{10}Ni_{10}$ ($10 \leq x \leq 60$). We find that the AFM state is lower in energy than the FiM state for almost all investigated alloys. Only for $Cr_{10}Mn_{10}Fe_{60}Co_{10}Ni_{10}$, the FiM state shows a slightly lower total energy as the AFM state (by about ~4 meV/atom). We also estimate T_c for the investigated alloys in the AFM state based on the mean-field approximation [52–54]. The obtained T_c are all within a range of 200~350 K i.e. close to room temperature considering that mean-field approximation usually overestimates T_c. The results also imply that, although the alloys are likely paramagnetic at room temperature, a substantial amount of magnetic SRO may be preserved which could, in principle, also alter the chemical trends. The computed T_c tends to decrease with Mn content, indicating that any potential magnetic SRO would be also less significant for Mn-deficient compositions.

The SFEs computed for the AFM state are shown in Fig. 8 (triangle green symbols). In the AFM state, the SFEs are found to be substantially higher than those in the PM state. This indicates that magnetic ordering increases the overall SFEs of the investigated alloys. It is also found that the SFE in the AFM state decreases with Mn content similar as also found for the PM state. From $Cr_{10}Mn_{50}Fe_{20}Co_{10}Ni_{10}$ to $Cr_{10}Mn_{10}Fe_{60}Co_{10}Ni_{10}$, the SFE in the AFM state decreases by approximately 160 mJ/m^2. One could speculate that at finite temperatures the SFE values are in between those in the AFM and in the PM states. Note that e.g. lattice vibrations may further shift the total SFEs as discussed above.

This significant reduction in the SFE with decreasing Mn content supports the experimental observations that twinning processes play an important role in the deformation of the NT-HEA ($Cr_{10}Mn_{10}Fe_{60}Co_{10}Ni_{10}$). A similar reduction in SFE is computationally also found for Ni-free $Cr_{10}Mn_xFe_{80-x}Co_{10}$ alloys [55] as well as for $Cr_{20}Mn_xFe_yCo_{20}Ni_z$ ($x + y + z = 60$) [51]. These findings support the experimental observations that by tuning the Mn content and hence the SFE, the deformation mode can be tailored to obtain desired mechanical properties in these HEAs.

4.2. Mechanical properties and underlying deformation mechanisms

For most polycrystalline metals and alloys, the improvement in strength by grain refinement is usually accompanied by the decrease in ductility. The increased strength can be explained by grain refinement and the higher fraction of grain boundaries, which impede dislocation motion. The relationship between yield strength and grain size can be described by the classical Hall-Petch relationship [56]:

$$\sigma_y = \sigma_0 + k_y \cdot d^{-1/2} \tag{4}$$

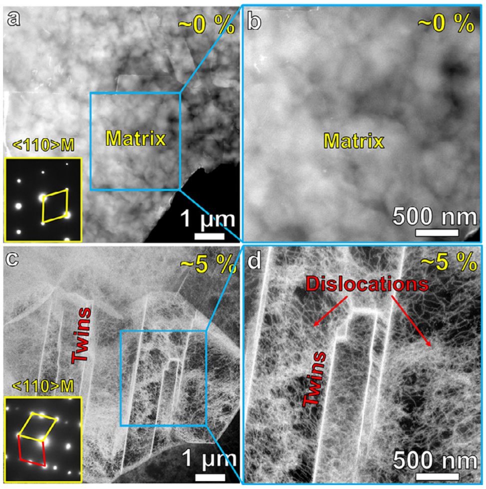

Fig. 9. Representative LAADF-STEM images of $Cr_{10}Mn_{10}Fe_{60}Co_{10}Ni_{10}$ NT-HEA with fine grain (FG) structure with true strain values: (a) and (b) ~0% prior to deformation; (c) and (d) ~5% after tensile deformation.

where σ_y is the yield stress, σ_0 describes the lattice friction stress, k_y is the strengthening coefficient and d describes the average grain diameter. According to Eq. (4), the increase of yield strength caused by grain refinement ($\Delta\sigma_G$) can be expressed as [56]:

$$\Delta\sigma_G = k_y\left(d_{FG}^{-1/2} - d_{CG}^{-1/2}\right) \tag{5}$$

In this work, $\Delta\sigma_G$is obtained from the stress-strain data. According to Eq. (4), the value of k_y for D-HEA is 517 MPa · μm$^{1/2}$ and the strengthening coefficient k_y for NT-HEA is 810 MPa · μm$^{1/2}$. The different strengthening coefficients for D-HEA and NT-HEA result in different yield strengths of two alloys.

The critical stress for twin growth τ_{tw}, can be estimated by the following equation [22]:

$$\tau_{tw} = \frac{\gamma_{ISF}}{3b_s} + \frac{3Gb_s}{L_0} \tag{6}$$

Here, L_0 is the width of twin embryo (260 nm) [22], and G is the shear modulus which was determined to be 76 GPa. The Burgers vector of the partial dislocation (b_s) is 0.147 nm. Different Mn contents of the two alloys result in quite different SFEs, which would lead to a difference in the twinning stress. For the D-HEA alloy, which has a high SFE, and the shear stress required to grow twins is ~300 MPa. By considering a Taylor factor of 3.06, a normal stress of ~920 MPa is required to grow twins the twinning stress, which is even higher than the UTS of D-HEA (FG), thus no twins could be observed in the deformed D-HEA (FG).

In order to study the initiation of twinning in NT-HEA, both calculations and TEM observations were used to estimate the initial strain of twinning. For NT-HEA with a lower SFE, the shear stress required to grow twins is ~130 MPa, and a normal stress of ~400 MPa is required to grow twins in NT-HEA. The measured yield strengths of NT-HEA (CG) and NT-HEA (FG) are 181 MPa and 314 MPa, thus the predicted stresses for twinning is mainly reached after yielding. This indicates that for the NT-HEA (FG), twins start to grow at ~5% of strain, as shown in point 1 of Fig. 3(a), contributing to hardening at the early stages of plastic deformation. LAADF-STEM images of the NT-HEA (FG) before and after deformation (Fig. 9) further support that true strain of ~5% leads to the formation of the twins (~645 ± 428 nm). Twin boundaries act as effective barriers for dislocation motion, where incoming dislocations may dissociate into two Shockley partials propagating along the twinning boundaries in opposite directions [57,58]. The interaction between dislocations and twin boundaries results in a high work-hardening ability, which explains the re-

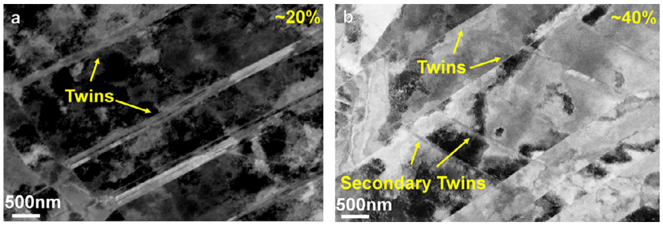

Fig. 10. ECC images of $Cr_{10}Mn_{10}Fe_{60}Co_{10}Ni_{10}$ NT-HEA with fine grain (CG) structure with true strain values: (a) ~20%; (b) 40% after tensile deformation.

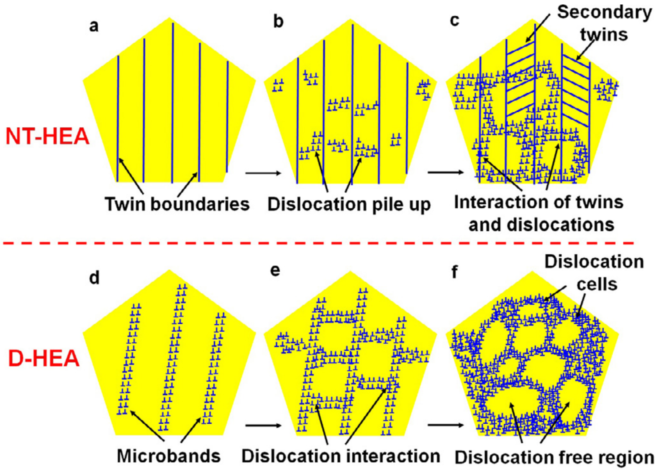

Fig. 11. Schematic showing the evolution of microstructures: (a) twin boundaries; (b) dislocation pile up; (c) interaction of twins and dislocations; (d) microbands composed of dislocation walls; (e) dislocations interactions; (f) dense dislocation cells.

tained high work hardening rate in region 1 of Fig. 3(d). Reaching the critical twinning stress in NT-HEA (FG) shortly after yielding results in an extended strain range where twinning can provide high steady work hardening, resulting in a high ultimate tensile strength [42,59].

For the NT-HEA (CG), the critical twinning stress is reached at a strain of about 20%, as shown in point 2 Fig. 3(a), indicating a delayed formation of deformation twins. The delayed interaction of dislocations and twins causes a slower decrease in the strain hardening rate and delayed retention of the work hardening rate, shown in region 2 of Fig. 3(d). ECC image of the NT-HEA (CG), as shown in Fig. 10(a), also supports that twins are formed with a true strain of ~20%. Thus, the onset of necking is shifted to higher strains resulting in an excellent ductility (~85%) of NT-HEA (CG). The excellent ductility could be explained by concurrent deformation mechanisms involving nano-twinning, related to the low SFE and dislocation-based plasticity. Based on the experimental observations, a schematic sequence of the deformation mechanisms of NT-HEA and D-HEA is plotted in Fig. 11.

For the NT-HEA, the low SFE promotes mechanical twinning (nucleating at initial dislocation pile-ups). Twinning can already be initiated at low strains (5%), as shown in Fig. 11(a), which is common in Fe–Mn austenitic steels [60]. At higher strains, dislocation slip is activated and further straining leads to interactions of mechanical twins and dislocations [61,62] as shown in Fig. 11(b). The twins act as barriers for dislocation glide leading to a further strain hardening. At higher strains dislocations cell structures evolve contributing to further strengthing and ductility. As deformation continues, secondary nano-twins are activated in the NT-HEA, as seen in Fig. 10(b) and Fig. 11(c), and the interaction of nano-twins and dislocations finally results in an excellent ductility of the NT-HEA at room temperature.

For the D-HEA, we find an approach to increase strength and ductility of single FCC phase high entropy alloys simultaneously. The increased ductility comes from the formation of microbands. Microbanding has been mainly studied in lightweight austenitic steels [24,63] and duplex steels [64], which was also observed in HEAs [65]. During the deformation of D-HEA, the grain first subdivides into several misoriented domains, resulting in the formation of microbands, as Fig. 11(d) shows. As deformation continues, the misorientation is increasing, leading to the formation of dense dislocation cell blocks, which is responsible for the improvement in the work hardening rate at higher strains (>7%). Meanwhile, the space between dislocation walls evolves into dislocation free regions, as is shown in Fig. 11(f), and these mobile dislocation cells [66,67] contribute to the plastic strain. As deformation continues, the formation of microbands relaxes plastic localization [68] and leads to an increase in ductility. As grain size decreases, more mobile dislocations are involved during deformation, thus both strength and ductility of D-HEA are improved simultaneously.

We develop two single FCC phase HEAs with different stacking fault energies (SFEs) tuned by the Mn content. The designed D-HEA with high SFE shows a dislocation dominated deformation mechanism, whereas, in the NT-HEA with its low SFE, twinning-induced plasticity is the major deformation mode. The effects of grain size on the tensile strength and ductility of the two HEAs were studied systematically. We observe that the high strength and ductility in the D-HEA is provided by dislocation multiplication and microband formation. The deformation mechanism of NT-HEA is dominated by nano-twinning and dislocation plasticity. The interaction between dislocations and twin boundaries results in a high work-hardening ability and an increased ductility. The influence of the Mn content on the SFE is explored by first principles calculations and can be used as a simple descriptor to explain the overall change in deformation modes. Reducing the SFE and refining the grain size as a second descriptor, enables the design of alloys erasing the strength-ductility tradeoff in single FCC phase HEAs. These parameters, SFE and grain size, can be used as design guidelines for other single phase HEAs to conceive alloy compositions with superior mechanical properties.

5. Conclusions

The mechanical properties of the two single-phase non-equiatomic HEAs, $Cr_{10}Mn_{50}Fe_{20}Co_{10}Ni_{10}$ (D-HEA: dislocation dominated-high entropy alloy) and $Cr_{10}Mn_{10}Fe_{60}Co_{10}Ni_{10}$ (at.%) (NT-HEA: twinning dominated-high entropy alloy), have been investigated. The effect of stacking fault energy on the mechanical properties and deformation mechanism is investigated. The main conclusions are:

(1) D-HEA and NT-HEA, both in homogenized and in recrystallized states, consist of a single FCC phase. Both two alloys have high phase stability and keep a single FCC phase after tensile deformation.
(2) In D-HEA, the grain refinement leads to increases in both strength and ductility. When grain size decreases from 347.5 ± 216.1 µm to 18.3 ± 9.3 µm, the ultimate tensile strength increases from 543±4 MPa to 621±8 MPa, and the elongation to failure enhances from 43±2% to 55±1%.
(3) In simulation, Mn content has a profound effect on the SFE of the investigated non-equiatomic HEAs. When the Mn content decreases from 50% to 10%, first-principles simulations predict the decrease of the SFE. The varying SFE has a great influence on the deformation mechanism found in experiments as described above. The first principle calculations can be used as a simple descriptor to explain the overall change in deformation modes.

(4) The deformation of D-HEA is dominated by microbanding, which act both as dislocation sources and dislocation barriers, eventually, leading to the formation of dislocation cell structures, which are responsible for the improvement in work hardening. The numerous dislocaton sources in the microbands are believed to erase the strength-ductility trade-off. The deformation of NT-HEA is dominated by nano-twinning, and the interaction between nano-twins and dislocations is beneficial for getting outstanding ductility of 85% engineering strain. These parameters can also be used in single FCC phase HEAs to conceive alloy compositions by tuning the stacking fault energy and grain size to tailor their mechanical properties.

Declaration of Competing Interests

We confirm that there are no conflicts of interest associated with this publication. We confirm that this manuscript has not been published nor submitted simultaneously elsewhere. We further confirm that all authors have checked the manuscript and have agreed to the submission.

Acknowledgments

Partial funding of this research by the Deutsche Forschungsgemeinschaft in the framework (Grant no. CL 2133/4-1 and KO 5080/2-1) of the Priority Programme “Compositionally Complex Alloys – High Entropy Alloys (CCA-HEA)” is gratefully acknowledged. The National Key Research and Development Program of China (Grant numbers 2018YFB0703400) is also acknowledged. The authors would like to gratefully thank B. Breitbach, V. Kree, M. Adamek, A. Bobrowski, P. Watermeyer, K. Angenendt and M. Nellessen at the Max-Planck-Institut für Eisenforschung for their excellent experimental support.

Appendix A

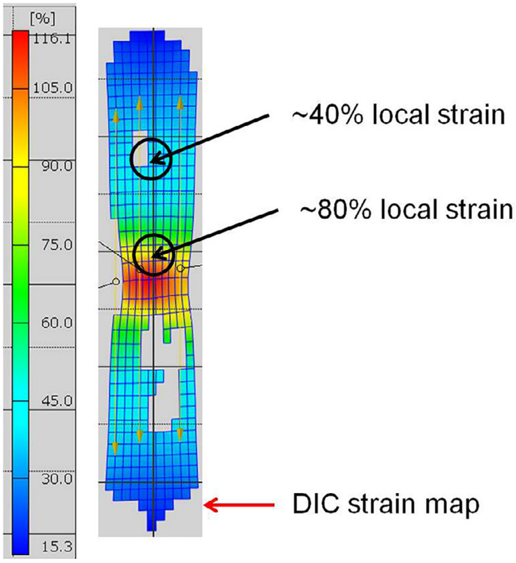

References

[1] D.B. Miracle, O.N. Senkov, A critical review of high entropy alloys and related concepts, Acta Mater. 122 (2017) 448–511.
[2] Y. Zou, S. Maiti, W. Steurer, R. Spolenak, Size-dependent plasticity in an $Nb_{25}Mo_{25}Ta_{25}W_{25}$ refractory high-entropy alloy, Acta Mater. 65 (2014) 85–97.
[3] Z.G. Zhu, K.H. Ma, Q. Wang, C.H. Shek, Compositional dependence of phase formation and mechanical properties in three CoCrFeNi-(Mn/Al/Cu) high entropy alloys, Intermetallics 79 (2016) 1–11.
[4] Y. Zhao, D.-.H. Lee, M.-.Y. Seok, J.-.A. Lee, M.P. Phaniraj, J.-.Y. Suh, H.-.Y. Ha, J.-.Y. Kim, U. Ramamurty, J.-i. Jang, Resistance of CoCrFeMnNi high-entropy alloy to gaseous hydrogen embrittlement, Scr. Mater. 135 (2017) 54–58.
[5] Á. Vida, N.Q. Chinh, J. Lendvai, A. Heczel, L.K. Varga, Microstructures and transition from brittle to ductile behavior of NiFeCrMoW high entropy alloys, Mater. Lett. 195 (2017) 14–17.
[6] C. Zhang, C. Zhu, T. Harrington, K. Vecchio, Design of non-equiatomic high entropy alloys with heterogeneous lamella structure towards strength-ductility synergy, Scr. Mater. 154 (2018) 78–82.
[7] Z. Zhang, M.M. Mao, J. Wang, B. Gludovatz, Z. Zhang, S.X. Mao, E.P. George, Q. Yu, R.O. Ritchie, Nanoscale origins of the damage tolerance of the high-entropy alloy crmnfeconi, Nat. Commun. 6 (2015) 10143.
[8] X. Wu, M. Yang, F. Yuan, G. Wu, Y. Wei, X. Huang, Y. Zhu, Heterogeneous lamella structure unites ultrafine-grain strength with coarse-grain ductility, Proc. Natl. Acad. Sci. U. S. A. 112 (47) (2015) 14501–14505.
[9] Z. Li, D. Raabe, Influence of compositional inhomogeneity on mechanical behavior of an interstitial dual-phase high-entropy alloy, Mater. Chem. Phys. 210 (2018) 29–36.
[10] Z. Li, F. Körmann, B. Grabowski, J. Neugebauer, D. Raabe, Ab initio assisted design of quinary dual-phase high-entropy alloys with transformation-induced plasticity, Acta Mater. 136 (2017) 262–270.
[11] H.T. Wang, N.R. Tao, Nano-twinned Fe-Mn alloy prepared by reverse martensitic phase transformation, Scr. Mater. 145 (2018) 109–112.
[12] Z. Li, C.C. Tasan, K.G. Pradeep, D. Raabe, A TRIP-assisted dual-phase high-entropy alloy: grain size and phase fraction effects on deformation behavior, Acta Mater. 131 (2017) 323–335.
[13] T. Li, T. Liu, L. Zhang, T. Fu, H. Wei, First-principles investigation on slip systems and twinnability of tic, Comput. Mater. Sci. 126 (2017) 103–107.
[14] L. Patriarca, A. Ojha, H. Sehitoglu, Y.I. Chumlyakov, Slip nucleation in single crystal FeNiCoCrMn high entropy alloy, Scr. Mater. 112 (2016) 54–57.
[15] A.J. Zaddach, R.O. Scattergood, C.C. Koch, Tensile properties of low-stacking fault energy high-entropy alloys, Mater. Sci. Eng.: A 636 (2015) 373–378.
[16] G. Meric de Bellefon, M.N. Gussev, A.D. Stoica, J.C. van Duysen, K. Sridharan, Examining the influence of stacking fault width on deformation twinning in an austenitic stainless steel, Scr. Mater. 157 (2018) 162–166.
[17] M.J. Yao, K.G. Pradeep, C.C. Tasan, D. Raabe, A novel, single phase, non-equiatomic femnnicocr high-entropy alloy with exceptional phase stability and tensile ductility, Scr. Mater. 72-73 (2014) 5–8.
[18] W. Lu, C.H. Liebscher, G. Dehm, D. Raabe, Z. Li, Bidirectional transformation enables hierarchical nanolaminate dual-phase high-entropy alloys, Adv. Mater. 30 (2018) 1804727.
[19] B. Cai, B. Liu, S. Kabra, Y. Wang, K. Yan, P.D. Lee, Y. Liu, Deformation mechanisms of Mo alloyed fecocrni high entropy alloy: in situ neutron diffraction, Acta Mater. 127 (2017) 471–480.
[20] Y.Y. Shang, Y. Wu, J.Y. He, X.Y. Zhu, S.F. Liu, H.L. Huang, K. An, Y. Chen, S.H. Jiang, H. Wang, X.J. Liu, Z.P. Lu, Solving the strength-ductility tradeoff in the medium-entropy NiCoCr alloy via interstitial strengthening of carbon, Intermetallics 106 (2019) 77–87.
[21] H. Kim, Strain hardening of novel high al low-density steel consisting of austenite matrix and B2-ordered intermetallic second phase in the perspective of non-cell forming face-centered-cubic alloy with high stacking fault energy, Scr. Mater. 160 (2019) 29–32.
[22] J. Su, D. Raabe, Z. Li, Hierarchical microstructure design to tune the mechanical behavior of an interstitial trip-twip high-entropy alloy, Acta Mater. 163 (2019) 40–54.
[23] N.L. Okamoto, S. Fujimoto, Y. Kambara, M. Kawamura, Z.M. Chen, H. Matsunoshita, K. Tanaka, H. Inui, E.P. George, Size effect, critical resolved shear stress, stacking fault energy, and solid solution strengthening in the Crmnfeconi high-entropy alloy, Sci. Rep. 6 (2016) 35863.
[24] I. Gutierrez-Urrutia, D. Raabe, Microbanding mechanism in an Fe-Mn-C high--Mn twinning-induced plasticity steel, Scr. Mater. 69 (1) (2013) 53–56.
[25] E. Welsch, D. Ponge, S.M. Hafez Haghighat, S. Sandlöbes, P. Choi, M. Herbig, S. Zaefferer, D. Raabe, Strain hardening by dynamic slip band refinement in a high-Mn lightweight steel, Acta Mater. 116 (2016) 188–199.
[26] L. Vitos, H.L. Skriver, B. Johansson, J. Kollár, Application of the exact muffin-tin orbitals theory: the spherical cell approximation, Comput. Mater. Sci. 18 (1) (2000) 24–38.
[27] L. Vitos, Total-energy method based on the exact muffin-tin orbitals theory, Phys. Rev. B 64 (1) (2001) 014107.
[28] A.V. Ruban, H.L. Skriver, Screened coulomb interactions in metallic alloys. I. Universal screening in the atomic-sphere approximation, Phys. Rev. B 66 (2) (2002) 024201.
[29] A.V. Ruban, S.I. Simak, P.A. Korzhavyi, H.L. Skriver, Screened coulomb interactions in metallic alloys. II. Screening beyond the single-site and atomic-sphere approximations, Phys. Rev. B 66 (2) (2002).
[30] L. Vitos, Computational Quantum Mechanics for Materials Engineers, Springer-Verlag, London, 2007.
[31] L. Vitos, J. Kollar, H.L. Skriver, Full charge-density calculation of the surface energy of metals, Phys. Rev. B Condens. Matter 49 (23) (1994) 16694–16701.
[32] L. Vitos, J. Kollár, H.L. Skriver, Full charge-density scheme with a kinetic-energy correction: application to ground-state properties of the 4d metals, Phys. Rev. B 55 (20) (1997) 13521–13527.
[33] J.P. Perdew, K. Burke, M. Ernzerhof, Generalized gradient approximation made simple, Phys. Rev. Lett. 77 (18) (1996) 3865–3868.
[34] P. Soven, Coherent-Potential model of substitutional disordered alloys, Phys. Rev. 156 (3) (1967) 809–813.

[35] B.L. Gyorffy, Coherent-Potential approximation for a nonoverlapping-muffin-t-in-potential model of random substitutional alloys, Phys. Rev. B 5 (6) (1972) 2382–2384.

[36] L. Vitos, I.A. Abrikosov, B. Johansson, Anisotropic lattice distortions in random alloys from first-principles theory, Phys. Rev. Lett. 87 (15) (2001).

[37] H. Huang, X. Li, Z. Dong, W. Li, S. Huang, D. Meng, X. Lai, T. Liu, S. Zhu, L. Vitos, Critical stress for twinning nucleation in CrCoNi-based medium and high entropy alloys, Acta Mater. 149 (2018) 388–396.

[38] D. Ma, B. Grabowski, F. Körmann, J. Neugebauer, D. Raabe, Ab initio thermodynamics of the cocrfemnni high entropy alloy: importance of entropy contributions beyond the configurational one, Acta Mater. 100 (2015) 90–97.

[39] P.J.H. Denteneer, W.v. Haeringen, Stacking-fault energies in semiconductors from first-principles calculations, J. Phys. C Solid State Phys. 20 (32) (1987) L883–L887.

[40] X. Zhang, B. Grabowski, F. Körmann, A.V. Ruban, Y. Gong, R.C. Reed, T. Hickel, J. Neugebauer, Temperature dependence of the stacking-fault Gibbs energy for Al, Cu, and Ni, Phys. Rev. B 98 (22) (2018) 224106.

[41] Y. Ikeda, B. Grabowski, F. Körmann, Ab initio phase stabilities and mechanical properties of multicomponent alloys: a comprehensive review for high entropy alloys and compositionally complex alloys, Mater. Char. 147 (2019) 464–511.

[42] G. Laplanche, A. Kostka, O.M. Horst, G. Eggeler, E.P. George, Microstructure evolution and critical stress for twinning in the CrMnFeCoNi high-entropy alloy, Acta Mater. 118 (2016) 152–163.

[43] Y. Deng, C.C. Tasan, K.G. Pradeep, H. Springer, A. Kostka, D. Raabe, Design of a twinning-induced plasticity high entropy alloy, Acta Mater. 94 (2015) 124–133.

[44] H. Cheng, H.Y. Wang, Y.C. Xie, Q.H. Tang, P.Q. Dai, Controllable fabrication of a carbide-containing FeCoCrNiMn high-entropy alloy: microstructure and mechanical properties, Mater. Sci. Technol. 33 (17) (2017) 2032–2039.

[45] J. Staunton, B.L. Gyorffy, A.J. Pindor, G.M. Stocks, H. Winter, The “disordered local moment” picture of itinerant magnetism at finite temperatures, J. Magn. Magn. Mater. 45 (1) (1984) 15–22.

[46] B.L. Gyorffy, A.J. Pindor, J. Staunton, G.M. Stocks, H. Winter, A first-principles theory of ferromagnetic phase transitions in metals, J. Phys. F Met. Phys. 15 (6) (1985) 1337–1386.

[47] C. Niu, C.R. LaRosa, J. Miao, M.J. Mills, M. Ghazisaeidi, Magnetically-driven phase transformation strengthening in high entropy alloys, Nat. Commun. 9 (1) (2018) 1363.

[48] S. Zhao, G.M. Stocks, Y. Zhang, Stacking fault energies of face-centered cubic concentrated solid solution alloys, Acta Mater. 134 (2017) 334–345.

[49] Y. Ikeda, F. Körmann, I. Tanaka, J. Neugebauer, Impact of chemical fluctuations on stacking fault energies of CrCoNi and CrMnFeCoNi high entropy alloys from first principles, Entropy 20 (9) (2018).

[50] S. Zhao, Y. Osetsky, G.M. Stocks, Y. Zhang, Local-environment dependence of stacking fault energies in concentrated solid-solution alloys, NPJ Comput. Mater. 5 (1) (2019).

[51] X. Wu, Z. Li, Y. Ikeda, B. Dutta, F. Körmann, J.r. Neugebauer, D. Raabe, private communications.

[52] K. Sato, L. Bergqvist, J. Kudrnovský, P.H. Dederichs, O. Eriksson, I. Turek, B. Sanyal, G. Bouzerar, H. Katayama-Yoshida, V.A. Dinh, T. Fukushima, H. Kizaki, R. Zeller, First-principles theory of dilute magnetic semiconductors, Rev. Mod. Phys. 82 (2) (2010) 1633–1690.

[53] F. Körmann, D. Ma, D.D. Belyea, M.S. Lucas, C.W. Miller, B. Grabowski, M.H.F. Sluiter, Treasure maps” for magnetic high-entropy-alloys from theory and experiment, Appl. Phys. Lett. 107 (14) (2015) 142404.

[54] Z. Rao, D. Ponge, F. Körmann, Y. Ikeda, O. Schneeweiss, M. Friák, J. Neugebauer, D. Raabe, Z. Li, Invar effects in FeNiCo medium entropy alloys: from an invar treasure map to alloy design, Intermetallics 111 (2019) 106520.

[55] S. Huang, H. Huang, W. Li, D. Kim, S. Lu, X. Li, E. Holmstrom, S.K. Kwon, L. Vitos, Twinning in metastable high-entropy alloys, Nat. Commun. 9 (1) (2018) 2381.

[56] J.Y. He, H. Wang, H.L. Huang, X.D. Xu, M.W. Chen, Y. Wu, X.J. Liu, T.G. Nieh, K. An, Z.P. Lu, A precipitation-hardened high-entropy alloy with outstanding tensile properties, Acta Mater. 102 (2016) 187–196.

[57] K. Lu, Stabilizing nanostructures in metals using grain and twin boundary architectures, Nat. Rev. Mater. 1 (5) (2016).

[58] H.T. Wang, N.R. Tao, K. Lu, Strengthening an austenitic Fe-Mn steel using nanotwinned austenitic grains, Acta Mater. 60 (9) (2012) 4027–4040.

[59] G. Laplanche, A. Kostka, C. Reinhart, J. Hunfeld, G. Eggeler, E.P. George, Reasons for the superior mechanical properties of medium-entropy CrCoNi compared to high-entropy CrMnFeCoNi, Acta Mater. 128 (2017) 292–303.

[60] J.H. Choi, M.C. Jo, H. Lee, A. Zargaran, T. Song, S.S. Sohn, N.J. Kim, S. Lee, Cu addition effects on trip to twip transition and tensile property improvement of ultra-high-strength austenitic high-Mn steels, Acta Mater. 166 (2019) 246–260.

[61] D.R. Steinmetz, T. Jäpel, B. Wietbrock, P. Eisenlohr, I. Gutierrez-Urrutia, A. Saeed–Akbari, T. Hickel, F. Roters, D. Raabe, Revealing the strain-hardening behavior of twinning-induced plasticity steels: theory, simulations, experiments, Acta Mater. 61 (2) (2013) 494–510.

[62] W.S. Choi, S. Sandlöbes, N.V. Malyar, C. Kirchlechner, S. Korte-Kerzel, G. Dehm, P.-P. Choi, D. Raabe, On the nature of twin boundary-associated strengthening in Fe-Mn-C steel, Scr. Mater. 156 (2018) 27–31.

[63] J.D. Yoo, K.-T. Park, Microband-induced plasticity in a high Mn-Al-C light steel, Mater. Sci. Eng.: A 496 (1–2) (2008) 417–424.

[64] S.S. Sohn, H. Song, B.-C. Suh, J.-H. Kwak, B.-J. Lee, N.J. Kim, S. Lee, Novel ultra--high-strength (ferrite + austenite) duplex lightweight steels achieved by fine dislocation substructures (Taylor lattices), grain refinement, and partial recrystallization, Acta Mater. 96 (2015) 301–310.

[65] Z. Wang, H. Bei, I. Baker, Microband induced plasticity and the temperature dependence of the mechanical properties of a carbon-doped FeNiMnAlCr high entropy alloy, Mater. Char. 139 (2018) 373–381.

[66] B.H.B.B. He, H.W. Yen, G.J. Cheng, Z.K. Wang, H.W. Luo, M.X. Huang, High dislocation density-induced large ductility in deformed and partitioned steels, Science 10 (2017) 1–8.

[67] K. Ming, X. Bi, J. Wang, Strength and ductility of CrFeCoNiMo alloy with hierarchical microstructures, Int. J. Plast. 113 (2018) 255–268.

[68] Z. Wang, I. Baker, Z. Cai, S. Chen, J.D. Poplawsky, W. Guo, The effect of interstitial carbon on the mechanical properties and dislocation substructure evolution in Fe 40.4 Ni 11.3 Mn 34.8 al 7.5 Cr 6 high entropy alloys, Acta Mater. 120 (2016) 228–239.